METALLURGY

Super-nano domains enable strength-conductivity synergy in copper foils

Zhao Cheng[1]†, Linhai Liu[1,2]†, Zhiyang Yu[3]†, Xiaoyuan Ye[3]†, Nairong Tao[1], Ting Zhu[4], Lei Lu[1]*

The development of copper foils that simultaneously exhibit ultrahigh strength, high electrical conductivity, and thermal stability remains a major challenge for advanced electronics and energy storage systems. We report a 10-micrometer-thick copper foil featuring nanoscale grains and periodically distributed gradient super-nano domains (approximately 3 nanometers in size) throughout its thickness that was produced by an industrially scalable electrodeposition process. This copper foil demonstrates a combination of approximately 900-megapascal tensile strength, 90% standard electrical conductivity, and exceptional thermal stability. These superior properties originate from a dual strengthening-stabilization mechanism in which the periodically distributed super-nano domains both enhance strength and stabilize grain boundaries. This strategy not only advances copper foil technology but also provides a general design pathway for developing other scalable, high-performance metallic materials.

Copper (Cu) foil serves as a critical current collector in lithium-ion batteries and as a primary conductive substrate in integrated circuits. The advancement of high-efficiency energy storage devices and artificial intelligence systems, together with the ongoing drive toward device miniaturization and weight reduction, has intensified the demand for increasingly thinner Cu foils (*1*–*3*). These applications require reliable performance under stringent mechanical and electrical conditions, placing greater emphasis on the foil's structural integrity and conductivity. However, achieving a combination of ultrahigh tensile strength, high ductility, electrical conductivity, and thermal stability in Cu foils remains a major challenge because these properties are often mutually exclusive (*4*–*6*).

This limitation stems from the widely used grain-refinement approach, which uses organic additives during electrodeposition to reduce grain size (*7*–*10*). However, grain refinement inherently couples these key properties in a competitive manner. Although this process strengthens the foil through the Hall-Petch effect (*4*, *11*–*13*), it simultaneously degrades electrical conductivity due to increased electron scattering at grain boundaries (GBs) (*5*, *6*, *14*). More critically, the gained strength is often short-lived: Nanograins (NGs) spontaneously coarsen at room temperature through self-annealing driven by the instability of high-energy GBs (*15*, *16*). This intrinsic instability, along with the associated loss of ductility, presents a fundamental barrier to achieving a balanced combination of mechanical and electrical properties.

Unlike conventional high-energy GBs, coherent twin boundaries (CTBs) can enhance strength through the Hall-Petch effect while preserving high electrical conductivity, offering a promising route to overcoming traditional trade-offs (*13*, *17*). However, fabricating nanotwinned Cu typically requires specialized low-current-density electrodeposition (*17*–*19*), which is incompatible with industrial high-speed production.

We introduce an impurity-engineering strategy (*20*, *21*) to produce high-performance, 10-μm-thick Cu foils through direct current electrodeposition at industrial current densities. Beyond conventional NGs, the Cu foil contains super-nano domains with a characteristic size in the range of 1 to 10 nm formed by the localized incorporation of additive-derived organic elements into the Cu matrix. These domains are arranged in a periodic gradient throughout the foil thickness. This gradient super-nano domain (GSD) architecture imparts an exceptional combination of ultrahigh strength, enhanced ductility, high electrical conductivity, and thermal stability.

Microstructure and chemistry

The GSD Cu foils (~10 μm thick) were fabricated through direct current electrodeposition in a $CuSO_4$ electrolyte under a constant current density of 650 mA/cm^2, meeting industrial production requirements. Mixed additives were used to enhance electrochemical polarization and to modulate the microstructure (see supplementary materials).

Cross-sectional scanning electron microscopy (SEM) (Fig. 1A) of the as-deposited Cu foil revealed a periodic layered structure evident as contrast bands perpendicular to the growth direction. Higher-magnification imaging (Fig. 1A, inset) showed columnar NGs spanning multiple layers with a characteristic wavelength (λ) of ~120 nm. Secondary ion mass spectrometry (SIMS) (Fig. 1A, inset) showed that these bands correlated with periodic fluctuations in C, O, and Cl concentrations. These elements originate from the deliberately introduced organic additives and KCl, the antagonistic effects (*10*) of which induce oscillations in electrode potential (fig. S1), thereby driving the periodic layering.

High-angle annular dark-field scanning transmission electron microscopy (HAADF-STEM) (Fig. 1B) revealed that the columnar grains exhibited a strong <110> texture (fig. S2), with an average short-axis diameter of ~60 nm and an aspect ratio of 2.7. The image further shows periodically distributed super-nano domains along the growth direction, consistent with the contrast modulation. This contrast originates from periodically distributed domain-lean regions (layer I, exhibiting conventional grain contrast) and domain-rich regions (layer II, appearing as dark dot-like features). Figure 1C shows that the spherical super-nano domains, with diameters of 2 to 6 nm (average ~3 nm), were predominantly embedded within layer II and distributed across both intra- and intergranular regions. Atomic-resolution imaging (Fig. 1C, inset) confirmed distortion-free lattices within the NG matrix, whereas the super-nano domains exhibited lower Z-contrast than the matrix.

HAADF-STEM tomography resolved the three-dimensional (3D) distribution of NGs and super-nano domains in the GSD Cu foil (Fig. 1D). In the 3D reconstruction, GBs are delineated by gray lines, and super-nano domains by red dots, defining the foil's characteristic microstructure. These domains maintain a continuous distribution across adjacent NGs in the *x*-*y* plane. Along the *z* axis, domain density varies markedly between layers I and II, with gradient architectures retained even within individual NGs. The volume fraction (*f*) of these domains oscillates sinusoidally from ~0 to ~8% along the *z* axis, with an average of ~3.2% across the foil thickness (Fig. 1E). To quantify this microstructural heterogeneity, we defined a structural gradient parameter (*S*) as the slope of the super-nano domain volume fraction with respect to depth, yielding $S = 113\%/\mu m$ for this GSD Cu foil, hereafter referred to as GSD-113.

Annular dark-field (ADF) (Fig. 1F) and integrated differential phase contrast (iDPC) (Fig. 1G) images revealed lattice distortions at the semi-coherent domain-matrix interface associated with dislocations, which became more evident under off-axis imaging conditions (fig. S3, A to F). Geometric phase analysis (GPA) (Fig. 1H) estimated local interfacial strains of ±5%, consistent with lattice distortion analysis of the semi-coherent boundary (Fig. 1I). Electron energy loss spectroscopy mapping (Fig. 1, J to L) confirmed the presence of organic elements (C and O) within the super-nano domains originating from additive-derived impurities.

[1]Shenyang National Laboratory for Materials Science, Institute of Metal Research, Chinese Academy of Sciences, Shenyang, China. [2]School of Materials Science and Engineering, University of Science and Technology of China, Shenyang, China. [3]State Key Laboratory of Green and Efficient Development of Phosphorus Resources, Fuzhou University, Fuzhou, China. [4]Woodruff School of Mechanical Engineering, Georgia Institute of Technology, Atlanta, GA, USA.
***Corresponding author. Email: llu@imr.ac.cn** †These authors contributed equally to this work.

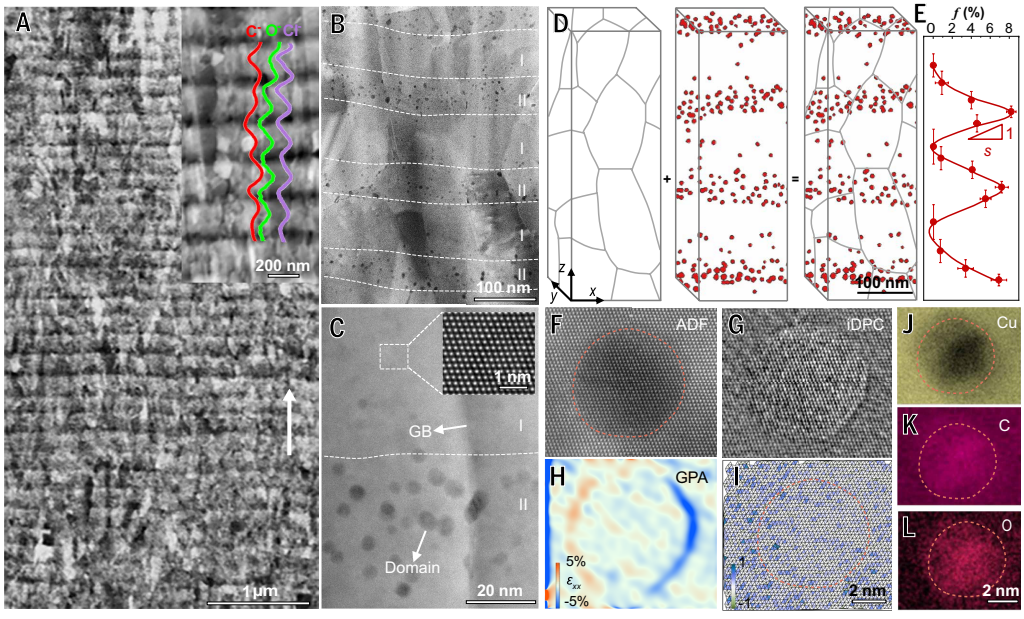

Fig. 1. Microstructure and chemistry of GSD Cu foils. (**A**) Cross-sectional SEM image. Inset shows a higher-magnification SEM image and the corresponding secondary ion mass spectrometry (SIMS) profiles with the distributions of C, O, and Cl along the depth. The growth direction is indicated by a white arrow. (**B**) Cross-sectional TEM image revealing periodically distributed GSDs. (**C**) Enlarged TEM image showing neighboring layers I and II. The inset shows the atomic structure of layer I. (**D**) TEM tomography reconstruction showing the 3D distribution of domains. The GBs of NGs are outlined. Both domains and GBs collectively constitute the GSD Cu microstructure. The *x*, *y*, and *z* axes correspond to the length (tensile), width, and thickness directions of the Cu foil, respectively. (**E**) Variation of domain volume fraction (*f*) along the depth. (**F** to **L**) Characterizations of a single domain in layer II through ADF imaging (F), iDPC analysis (G), GPA analysis (H), experimentally extracted atomic strain map (I), and electron energy loss spectroscopy maps of Cu (J), C (K), and O (L). Panels (F) to (I) and panels (J) and (L) share the same scale bars.

Diffraction patterns from the super-nano domains and the adjacent Cu matrix were nearly identical (fig. S3, G and H), confirming their shared face-centered cubic (FCC) structure. Glow discharge mass spectrometry measurements (table S1) showed that the total impurity content in the Cu foil was extremely low (~0.09 wt %), maintaining high Cu purity (99.91 wt %). The architecture of intra- and intergranular GSDs, with a periodicity as small as ~100 nm in Cu foils, was achieved through an impurity-engineering strategy.

The gradient microstructure of GSD Cu foils exhibits high tunability through precise control of composite additive concentrations. By reducing the additive concentration, we fabricated two additional Cu foils, GSD-68 and GSD-42, with similar nanocrystalline matrices but lower structural gradients (68 and 42%/μm, respectively; Table 1 and fig. S4). Both foils displayed lower domain volume fractions (1.7 and 1.0%, respectively) and slightly larger grain sizes. For comparison, we also prepared a reference Cu foil with randomly distributed (RD) super-nano domains (1.5% volume fraction; fig. S5) and a domain-free NG Cu foil with a comparable grain size (~61 nm; fig. S6A).

Synergy of multiple properties

Tensile stress-strain curves (Fig. 2A) showed that domain-containing Cu foils (GSD and RD) exhibited substantially higher strength than the domain-free NG Cu foil (630 MPa in the as-prepared state), consistent with the Hall-Petch effect (*13*). The periodically distributed GSD in foils confers a strength-ductility synergy. As the structural gradient increased from 42 to 113%/μm, the tensile strength of GSD Cu foils increased from 688 ± 33 to 889 ± 6 MPa, whereas elongation increased slightly. The GSD-113 foil, with the highest structural gradient, achieved the greatest strength and elongation. By contrast, the RD Cu foil, with a domain fraction and initial yielding behavior similar to GSD-68, underwent premature fractures, limiting its strength (701 MPa) and elongation (~1.8%).

Table 1. Microstructure characteristic length and tensile properties of GSD, RD, and conventional NG Cu foils.

Cu foil	d_G (nm)	d_D (nm)	S (%/μm)	f (%)	σ_{uts} (MPa)	δ_f (%)
GSD-113	60 ± 3	3.0 ± 0.1	113	3.2	889 ± 6	3.2 ± 0.3
GSD-68	71 ± 3	3.3 ± 0.1	68	1.7	761 ± 27	2.9 ± 0.2
GSD-42	80 ± 2	3.1 ± 0.1	42	1.0	688 ± 33	2.8 ± 0.3
RD	77 ± 2	3.4 ± 0.1	—	1.5	701 ± 12	1.8 ± 0.1
NG	61 ± 2	—	—	—	630 ± 27	2.4 ± 0.2

d_G, grain size; d_D, domain size; S, structural gradient; f, overall volume fraction of domains; σ_{uts}, ultimate tensile strength; δ_f, elongation

GSD-113 exhibited exceptional thermal stability, retaining nearly 100% of its original strength after prolonged storage (up to 180 days at room temperature; Fig. 2B). Hardness measurements confirmed this stability, with the foil maintaining an ultrahigh hardness of 2.7 GPa throughout the entire testing period (fig. S7B). Microstructural analysis (figs. S6 and S7A) also supported these findings, revealing no detectable changes in grain size or domain configuration during extended storage. Tensile tests after elevated-temperature annealing (150°C for 10 min in ambient atmosphere; fig. S8) further confirmed the superior stability.

By contrast, NG Cu foils exhibited pronounced strength degradation (~50% loss within 24 hours; Fig. 2B) and hardness reduction (from 1.9 to 1.2 GPa; fig. S7B), accompanied by rapid grain coarsening from ~60 nm to ~3 μm due to self-annealing. RD Cu foils, by comparison, retained stable mechanical properties after storage for up to 180 days at room temperature (fig. S7C).

Figure 2C compares the strength-elongation performance of GSD, RD, and conventional Cu foils of comparable thickness (*7*, *8*, *22*–*26*).

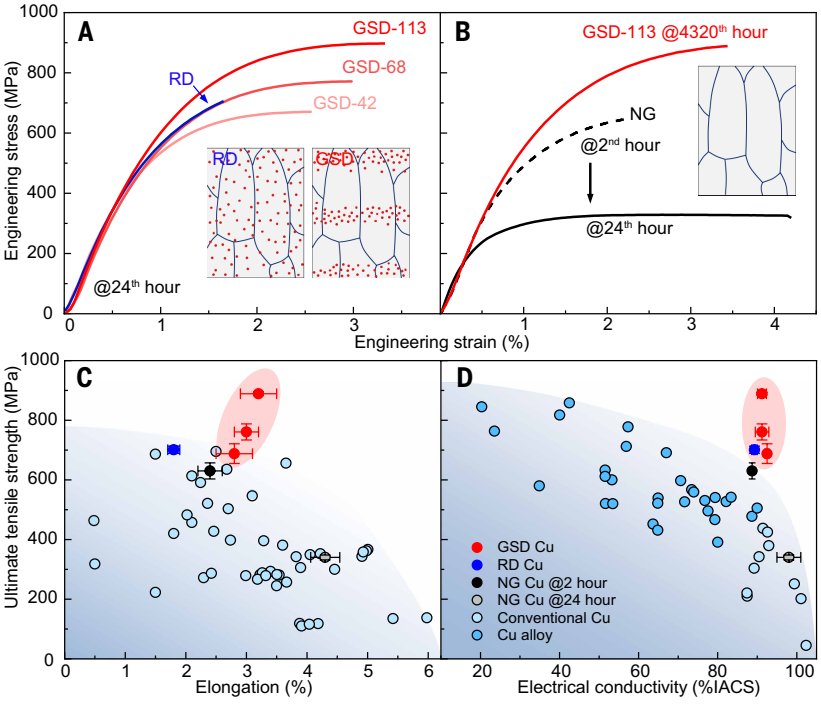

Fig. 2. Mechanical and electrical properties of GSD Cu foils. (**A**) Engineering tensile stress-strain curves of GSD-42, GSD-68, and GSD-113 compared with RD Cu foil after 24 hours of processing. (**B**) Long-term mechanical stability of GSD-113 showing its tensile behavior after 4320 hours (180 days) compared with NG Cu foils after 2 and 24 hours. Schematic illustrations in the insets depict the characteristic microstructural configurations for GSD, RD, and NG Cu foils. (**C** and **D**) Comparison of ultimate tensile strength versus elongation (C) and electrical conductivity (D) of GSD Cu foils with those of RD Cu foils, conventional Cu foils (*7*,*8*,*22*–*26*), and Cu alloys (*27*–*29*).

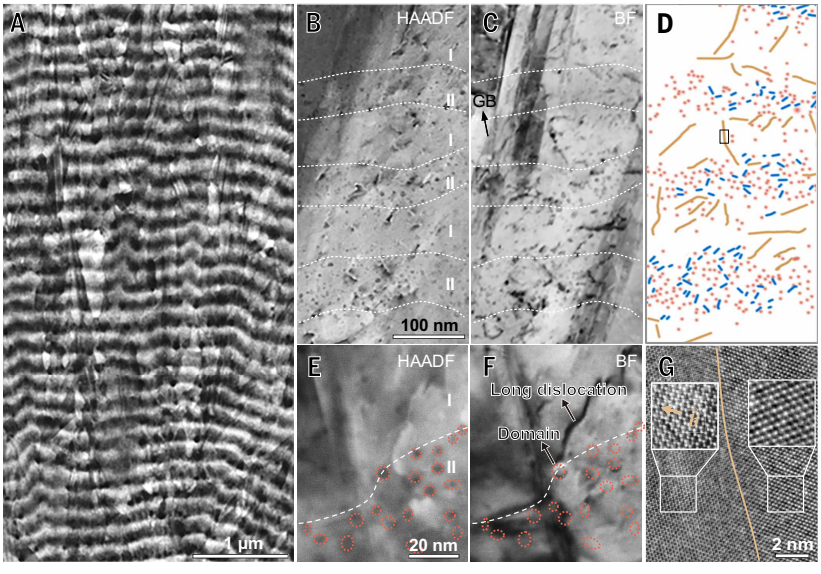

Fig. 3. Deformed microstructure of GSD-113. (**A**) Cross-sectional SEM image near the fracture region. (**B** and **C**) HAADF and BF images revealing the distribution of domains and dislocations. (**D**) Schematic illustration showing the superposition of domains and dislocations derived from (B) and (C), where domains, long dislocations in layer I, and short dislocations in layer II are outlined in red, orange, and blue, respectively. (B) to (D) share the same scale bar. (**E** and **F**) HAADF and BF images showing long dislocations pinned by domains between layers I and II. (**G**) Magnified iDPC image of the region marked by the box in (D), including a long dislocation. Insets in (G) display the atomic structures of the sheared (left) and unsheared (right) regions, with the Burgers vector indicated by an arrow.

Conventional Cu foils exhibited a strength limit of ~700 MPa and displayed the typical trade-off with elongation, a trend also observed in RD Cu foils. GSD Cu foils surpassed this limit, achieving a strength of ~900 MPa without sacrificing ductility. The elongation of GSD Cu foils (~3%) matches that of standard thin foils, where thickness limits work hardening, yet remains fully adequate for demanding applications such as lithium-ion battery current collectors.

Figure 2D illustrates the strength-conductivity trade-off in conventional Cu and Cu alloys (*27*–*29*). NG Cu foils showed improved conductivity from ~90 to ~98% IACS (International Annealed Copper Standard) after 24 hours of storage at room temperature, but this improvement came at the expense of strength degradation due to self-annealing. By contrast, both RD and GSD Cu foils maintained high conductivity (~90% IACS) comparable to that of freshly prepared NG Cu foils, indicating minimal electron scattering from super-nano domains. Overall, the GSD-113 foil achieved a combination of ultrahigh strength (~900 MPa), excellent electrical conductivity (~90% IACS), enhanced elongation, and exceptional thermal stability, a property set not observed in other high-performance foils or bulk metallic materials (*5*, *6*).

Dislocation mechanisms

To elucidate the strengthening mechanisms in GSD architectures, we examined the deformation behavior of the fractured GSD-113 foil, which was selected for its pronounced structural gradient and superior properties. SEM imaging (Fig. 3A) revealed continuous plastic deformation throughout the layered structure along the *x*-*y* and *z* directions without cracking or strain localization at GBs or interlayer interfaces. Compared with the initially straight layers (Fig. 1A), the deformed structure became wavy. HAADF imaging (Fig. 3B) resolved the distribution of super-nano domains (dark dots), whereas bright-field (BF) imaging (Fig. 3C) revealed the dislocation configurations (dark lines) within the deformed GSD-113 foil. Their superposition (Fig. 3D) revealed a pronounced difference in dislocation behavior: Layer I hosted extended dislocation networks (long orange lines) with a relatively low density of ~10^{15} m^{-2}, whereas layer II contained dense populations (~10^{16} m^{-2}) of short dislocations (blue lines).

HAADF and BF images (Fig. 3, E and F) showed that long dislocations were confined to layer I and pinned by super-nano domains. iDPC analysis (Fig. 3G) revealed distinct contrast along an extended dislocation, distinguishing perfect lattice regions from faulted areas with superimposed, shifted lattices. The inset in Fig. 3G identifies a 1/6<112> displacement, confirming predominant edge-type Shockley partial dislocations. Aberration-corrected STEM imaging of layer II (Fig. 4A) resolved dense short dislocations within the domain-rich region. A high density (~10^{16} m^{-2}) of short dislocations (blue circles) was concentrated around the super-nano domains, with occasional edge dislocations and stacking faults bounded by partial dislocations. This density far exceeds the typical upper limit (~10^{15} m^{-2}) for conventional homogeneous or heterogeneous FCC metals, including Cu and its alloys (*19*, *30*–*33*).

Figure 4B reveals the atomic-scale structure of short dislocations interacting with super-nano domains. A magnified view (Fig. 4C) shows distorted atomic arrangements along the dislocation core, in contrast to

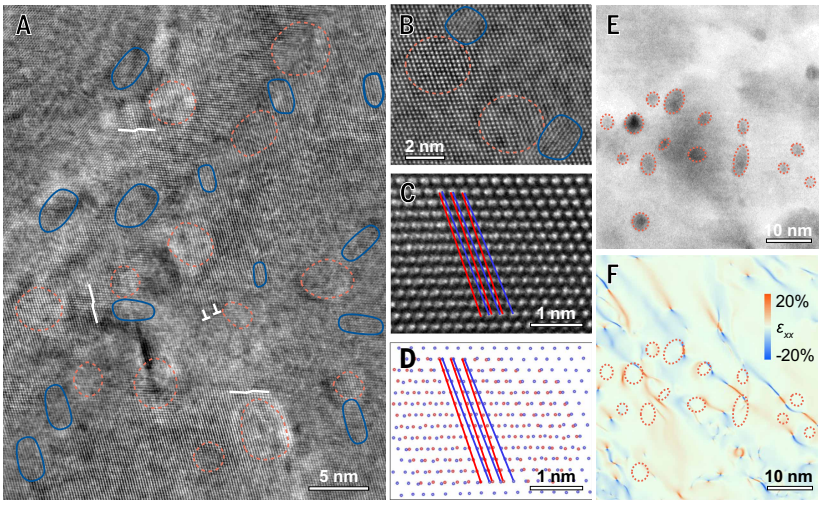

Fig. 4. Dislocation behavior in layer II of GSD-113. (**A**) Atomistic iDPC-STEM image showing high-density short dislocation segments (blue circles) distributed around super-nano domains (dotted circles). Edge dislocations and stacking faults are indicated by white ⊥ symbols and polylines, respectively. (**B**) Magnified view showing short dislocation segments. (**C** and **D**) Atomic-resolution image and corresponding reconstructed atomic model of a representative short dislocation segment, confirming its predominant screw character. (**E** and **F**) HAADF image and GPA strain map of layer II enriched with super-nano domains. The color contour represents the distribution of atomic strain (ε_{xx}).

the coherent lattice in adjacent regions. Some screw segments bridged neighboring domains or intersected with stacking faults, whereas others were associated with a single super-nano domain or appear isolated, likely terminating at the TEM foil surface or intersecting with dislocations outside of the current imaging conditions. Figure 4D reveals spiral steps with zigzag displacements along short dislocations, indicating a predominant screw character. This assignment was supported by the Burgers vectors ($\mathbf{b} = 1/2\langle 110\rangle$) and atomic-scale structural analysis (fig. S9). This behavior contrasts with the edge character of the long partial dislocations in layer I, indicating that short screw dislocations are primarily active in layer II. Correlative HAADF imaging and GPA strain mapping (Fig. 4, E and F) revealed localized strain along ~45° to the tensile direction (x axis), corresponding to the maximum shear stress direction. This strain (~20%) accumulated preferentially on one side of the domains and coincided with high-density dislocations, confirming the domains' strong pinning effect.

Discussion

GBs in metallic materials play a crucial role in governing mechanical strength. The well-established Hall-Petch relationship characterizes GB strengthening, indicating that yield strength increases with the inverse square root of grain size (*4*, *12*, *13*). This "smaller-is-stronger" principle has stimulated extensive research on NG metals because of their superior strength (*4*, *11*, *12*). However, NG metals also present notable drawbacks, including reduced ductility and electrical conductivity (*28*, *34*). When grain size falls below a critical threshold, softening arises from spontaneous GB migration (*15*), which is manifested as room-temperature self-annealing in Cu foils (Fig. 2B). This microstructural instability stems from the high excess energy stored within dense GB networks. A common metallurgical strategy to stabilize GBs involves alloying, whereby metallic solutes preferentially segregate to GBs, improving mechanical stability. Although effective in strengthening, this approach simultaneously degrades electrical conductivity through strong electron scattering from GB-segregated atoms (*5*, *6*).

In contrast to conventional strengthening strategies, which rely on heavy metallic solutes (e.g., Cr, Zr, and Ni) (*35*–*39*), electrodeposition often involves light organic elements (e.g., C, O, and Cl) derived from additives. These additives are used to control microstructures and optimize properties through electrochemical polarization effects (*7*, *11*). Although the unintentional incorporation of such light elements into grains or GBs has traditionally been regarded as detrimental (*40*), we show here that their controlled incorporation is advantageous. It produces super-nano domains with a homogeneous in-plane distribution and a periodic gradient throughout the foil thickness. This imparts exceptional GB thermal stability together with a combination of ultrahigh strength and high conductivity (Fig. 2).

The domain-mediated GB stabilization is attributed to two complementary mechanisms: (i) thermodynamic stabilization through bonding between Cu atoms and segregated light elements (C and O) at GBs (*41*, *42*) and (ii) kinetic stabilization through Zener pinning (*43*) of GBs by the super-nano domains. The architecture's pinning capability arises from the ultrahigh density of super-nano domains within layer II and the nanoscale spacing (~60 nm) between adjacent domain-rich layers, which collectively suppress GB migration.

In addition to stabilizing GBs, the GSD architecture, with super-nano domains distributed throughout both intra- and intergranular regions, contributes to the simultaneous realization of ultrahigh strength and enhanced ductility. The in-plane (x-y) intergranular distribution of super-nano domains in GSD Cu foils promotes uniform deformation, in contrast to conventional NG Cu, in which dislocation-GB interactions and the resulting GB migration induce strain localization and premature failure (*4*, *15*, *34*). Under mechanical loading, super-nano domains in layer II act as primary dislocation obstacles with an average spacing of ~7 nm, an order of magnitude smaller than the grain size, indicating that domain spacing predominantly governs the high flow stress. These domains mediate plastic deformation through two key roles: (i) promoting uniform stress and strain partitioning among NGs through their homogeneous in-plane distribution and (ii) trapping dislocations within grain interiors to reduce dislocation-GB interactions and mitigate strain localization (*36*, *38*).

Postdeformed foil exhibits continuous, crack-free deformation (Fig. 3A). The layers develop local wavy features along the structural gradient direction, a phenomenon rarely observed in conventional gradient (*19*, *44*, *45*) or laminated (*30*, *46*) nanostructures. This distinctive morphology could be attributed to the intragranular gradient distribution of super-nano domains along the foil thickness (i.e., the long axis of the columnar grains). Such an intragranular gradient promotes efficient slip transfer between adjacent layers within individual grains, unlike intergranular gradients, which typically cause dislocation pileup and strain localization at GBs (*19*, *30*, *44*–*46*).

The strain delocalization enabled by the GSD architecture provides favorable conditions for through-thickness gradient deformation (*47*). The disparity in domain density between layers I and II induces a plastic strain gradient along the thickness direction. The higher domain density in layer II confers greater dislocation resistance, delaying yielding and restricting plastic strain, whereas layer I undergoes more extensive deform. This difference generates a pronounced plastic strain gradient between the layers. According to strain gradient plasticity theory (*48*), geometrically necessary dislocations form to accommodate this strain gradient and maintain geometrical compatibility. These dislocations promote a strength-ductility synergy, giving heterogeneous nanostructures superior performance over their homogeneous counterparts (*19*, *30*, *44*–*46*).

As shown in Figs. 3 and 4, GSD-113 exhibited an exceptionally high dislocation density of ~10^{16} m^{-2}, which is about two orders of magnitude higher than that of the RD Cu foil (5×10^{14} m^{-2}; fig. S10), confirming the critical role of the GSD architecture in enhancing dislocation

storage capacity. This dislocation density also surpasses those reported for other heterogeneous nanostructures (*19*, *30*, *44*–*46*). The enhanced dislocation storage capacity arises from the intragranular GSD architecture in GSD-113, characterized by a super-nano domain structural gradient with a characteristic length scale of only ~60 nm (Fig. 1), which is two to three orders of magnitude smaller than conventional intergranular gradients typically observed at micrometer to millimeter scales (*19*, *30*, *44*–*46*).

Microscopy analyses (Figs. 3 and 4) revealed a synergistic dislocation mechanism that sustains plasticity within the GSD architecture. Plastic flow in domain-lean layer I is governed by the glide of long-edge dislocations, the predominance of which in NG FCC metals with medium to low stacking fault energy stems from their lower energy barriers compared with screw dislocations. Confined to their slip planes, these edge and mixed dislocations are readily pinned by super-nano domains in layer I (Fig. 3, E and F). By contrast, plasticity in layer II is largely sustained by screw dislocations. Their ability to undergo cross-slip (*49*) allows them to change slip planes, escape domain pinning, and accommodate further plastic deformation (Fig. 4B). With increasing load, the high local stresses generated near the dense super-nano domains likely enhance the activity of screw dislocations. Furthermore, the dense domains shorten the mean free path of screw dislocations, elevating dislocation densities to accommodate both the global strain and the associated strain gradients between layers I and II.

The ultrahigh dislocation storage capacity arising from intragranular gradients of super-nano domains provides additional strengthening beyond the individual contributions from stabilizing GBs and domain strengthening, collectively leading to ultrahigh strength (Fig. 2). Complex interactions among these ultrahigh-density dislocations further enhance the strain-hardening capacity (fig. S11) (*50*), allowing GSD Cu foils to retain considerable ductility compared with their NG and RD counterparts. Both strengthening and work hardening intensify with increasing structural gradient, thereby establishing a pathway to overcome the conventional strength-ductility trade-off in Cu foils relying solely on GB strengthening.

Based on the experimental results (Fig. 2D), GBs constitute the primary factor reducing the electrical conductivity of GSD Cu, whereas impurities play a minimal role. This behavior arises from the inherently low impurity content, with impurities preferentially segregated within the super-nano domains. Such segregation effectively purifies the Cu matrix, thereby minimizing electron-impurity scattering. High electrical conductivity is further preserved by key structural features, including the semicoherent interfaces of the super-nano domains (Fig. 1I) and the columnar grain morphology, which reduces GB density relative to equiaxed microstructures.

In summary, we have engineered a nanostructure in Cu foils comprising nanoscale grains and periodically distributed GSDs through direct current electrodeposition. This GSD architecture stabilizes GBs and achieves a combination of ultrahigh strength, excellent thermal stability, and exceptional electrical conductivity. These results address the challenges of self-annealing and the conventional strength-conductivity trade-off in Cu foils. Because of its extremely low impurity content and its full compatibility with industrial electrodeposition processes, the GSD design provides a cost-effective and industrially scalable route for producing high-performance conductive materials.

REFERENCES AND NOTES

1. M. Wu *et al.*, *Nature* **581**, 406–410 (2020).
2. H. Y. Hsiao *et al.*, *Science* **336**, 1007–1010 (2012).
3. Z. Zhang, Y. Song, B. Zhang, L. Wang, X. He, *Adv. Energy Mater.* **13**, 2302134 (2023).
4. M. A. Meyers, A. Mishra, D. J. Benson, *Prog. Mater. Sci.* **51**, 427–556 (2006).
5. K. Yang *et al.*, *Prog. Mater. Sci.* **138**, 101141 (2023).
6. S. Z. Han, E. A. Choi, S. H. Lim, S. Kim, J. Lee, *Prog. Mater. Sci.* **117**, 100720 (2021).
7. C. Liu, X. Chen, Z. Cheng, L. Lu, *Electrochim. Acta* **531**, 146330 (2025).
8. Y. Sun *et al.*, *Electrochim. Acta* **466**, 143068 (2023).
9. L. L. Lu *et al.*, *Rare Met.* **44**, 757–792 (2025).
10. P. Broekmann *et al.*, *Electrochim. Acta* **56**, 4724–4734 (2011).
11. P. Xu *et al.*, *Chem. Eng. J.* **484**, 149557 (2024).
12. J. Schiøtz, K. W. Jacobsen, *Science* **301**, 1357–1359 (2003).
13. Z. C. Cordero, B. E. Knight, C. A. Schuh, *Int. Mater. Rev.* **61**, 495–512 (2016).
14. A. F. Mayadas, M. Shatzkes, *Phys. Rev., B, Solid State* **1**, 1382–1389 (1970).
15. J. M. E. Harper *et al.*, *J. Appl. Phys.* **86**, 2516–2525 (1999).
16. K. Lu, *Nat. Rev. Mater.* **1**, 16019 (2016).
17. L. Lu, Y. Shen, X. Chen, L. Qian, K. Lu, *Science* **304**, 422–426 (2004).
18. D. P. Tran *et al.*, *Electrochim. Acta* **389**, 138640 (2021).
19. Z. Cheng, H. Zhou, Q. Lu, H. Gao, L. Lu, *Science* **362**, eaau1925 (2018).
20. I. Matsui, T. Uesugi, Y. Takigawa, K. Higashi, *Acta Mater.* **61**, 3360–3369 (2013).
21. Q. Huang, *J. Electrochem. Soc.* **165**, D251–D257 (2018).
22. C. Dai *et al.*, *Eng. Fail. Anal.* **101**, 193–205 (2019).
23. Z. Dong *et al.*, *J. Mater. Res. Technol.* **23**, 4268–4279 (2023).
24. X. Q. Yin *et al.*, *Rare Met.* **35**, 909–914 (2016).
25. Z. G. Li, L. Y. Gao, Z. Li, R. Sun, Z. Q. Liu, *J. Mater. Sci.* **57**, 17797–17811 (2022).
26. J. Zhu, J. Feng, Z. Guo, *RSC Adv.* **4**, 57671–57678 (2014).
27. K. P. Lee *et al.*, *Mater. Sci. Eng. A* **891**, 145990 (2024).
28. Y. Zhang, Y. S. Li, N. R. Tao, K. Lu, *Appl. Phys. Lett.* **91**, 211901 (2007).
29. R. Feng *et al.*, *Materials* **15**, 2249 (2022).
30. X. Ma *et al.*, *Acta Mater.* **116**, 43–52 (2016).
31. T. Ungár, E. Schafler, P. Hanák, S. Bernstorff, M. Zehetbauer, *Mater. Sci. Eng. A* **462**, 398–401 (2007).
32. D. A. Hughes, N. Hansen, *Acta Mater.* **148**, 374–383 (2018).
33. U. Essmann, H. Mughrabi, *Philos. Mag. A Phys. Condens. Matter Defects Mech. Prop.* **40**, 731–756 (1979).
34. C. C. Koch, D. G. Morris, K. Lu, A. Inoue, *MRS Bull.* **24**, 54–58 (1999).
35. F. Wang *et al.*, *Science* **384**, 1017–1022 (2024).
36. S. Jiang *et al.*, *Nature* **544**, 460–464 (2017).
37. W. Sun *et al.*, *Science* **363**, 972–975 (2019).
38. X. Wu *et al.*, *Sci. Rep.* **5**, 11728 (2015).
39. G. Wu, K. C. Chan, L. Zhu, L. Sun, J. Lu, *Nature* **545**, 80–83 (2017).
40. M. Yamaguchi, M. Shiga, H. Kaburaki, *Science* **307**, 393–397 (2005).
41. Z. Li *et al.*, *Nat. Commun.* **13**, 5581 (2022).
42. W. Huang, *Acc. Chem. Res.* **49**, 520–527 (2016).
43. K. Chang, W. Feng, L. Q. Chen, *Acta Mater.* **57**, 5229–5236 (2009).
44. T. H. Fang, W. L. Li, N. R. Tao, K. Lu, *Science* **331**, 1587–1590 (2011).
45. Q. Pan *et al.*, *Science* **374**, 984–989 (2021).
46. M. Göken, H. W. Höppel, *Adv. Mater.* **23**, 2663–2668 (2011).
47. L. Liu, C. Liu, J. Zheng, Z. Cheng, L. Lu, *Scr. Mater.* **271**, 116973 (2026).
48. H. Gao, Y. Huang, W. D. Nix, J. W. Hutchinson, *J. Mech. Phys. Solids* **47**, 1239–1263 (1999).
49. J. P. Hirth, J. Lothe, *Theory of Dislocations* (Wiley, ed. 2, 1982).
50. U. F. Kocks, H. Mecking, *Prog. Mater. Sci.* **48**, 171–273 (2003).

ACKNOWLEDGMENTS

We thank X. C. Chen for help with sample preparation. **Funding:** L. Lu acknowledges financial support from the National Natural Science Foundation of China (NSFC grants 92463302 and U24A2027), the project of Global Common Challenges (grant 172GJHZ2023075GC), and the Chinese Academy of Sciences (CAS). Z.C. acknowledges financial support from the NSFC (grants 52422102 and 52371124), the National Key R&D Program of China (grant 2024YFA1210600), and the Youth Innovation Promotion Association of CAS. Z.Y. acknowledges financial support from the NSFC (grant 52222102). **Author contributions:** L. Lu initiated and supervised the project. Z.C. and L. Liu prepared the sample, performed the experimental tests, and conducted SEM observations. Z.Y. and X.Y. conducted TEM observations. Z.C. and L. Lu designed the experiments and drafted the manuscript. All authors contributed to the discussions and revised the manuscript. **Competing interests:** The authors declare no competing interests. **Data, code, and materials availability:** All data generated or analyzed during this study are included in the main text or the supplementary materials. All raw materials used in the virgin make-up solution and additives were purchased from Sinopharm Chemical Reagent Co., Ltd.

SUPPLEMENTARY MATERIALS

science.org/doi/10.1126/science.aed7758
Materials and Methods; Figs. S1 to S11; Table S1; References (*51*–*55*)

Submitted 10 November 2025; accepted 9 February 2026

10.1126/science.aed7758

Super-nano domains enable strength-conductivity synergy in copper foils

Zhao Cheng, Linhai Liu, Zhiyang Yu, Xiaoyuan Ye, Nairong Tao, Ting Zhu, and Lei Lu

Science **392** (6795), . DOI: 10.1126/science.aed7758

Editor's summary

Although there are many ways to enhance individual properties in a metal, achieving a combination of ultrahigh tensile strength, high ductility, electrical conductivity, and thermal stability in copper is a challenge because these properties are often mutually exclusive. Cheng *et al*. showed that the incorporation of organic additives can lead to the stabilization of a layered microstructural architecture that features periodically distributed super-nano domains. The 10-micrometer-thick foils are produced through an industrially scalable electrodeposition process, which thus holds substantial promise for making foils for lithium-ion batteries and integrated circuits. —Marc S. Lavine